# The importance of anisotropic viscosity in numerical models for olivine textures in shear and subduction deformations

Yijun Wang[1 2], yijun0509wang@gmail.com
Ágnes Király[1 2], agnes.kiraly@geo.uio.no
Clinton P. Conrad[1 2], c.p.conrad@geo.uio.no
Lars N. Hansen[3], lnhansen@umn.edu
Menno Fraters[4], menno.fraters@tutanota.com

*[1]PHAB, University of Oslo, Oslo, Norway*
*[2]CEED, University of Oslo, Oslo, Norway*
*[3] University of Minnesota, Minneapolis, MN, USA*
*[4]University of California Davis, Davis, CA, USA*

# The importance of anisotropic viscosity in numerical models for olivine textures in shear and subduction deformations

Y. Wang[1 2], Á. Király[1 2], C.P. Conrad[1 2], L.N. Hansen[3], M. Fraters[4]

*[1]PHAB, University of Oslo, Oslo, Norway*
*[2]CEED, University of Oslo, Oslo, Norway*
*[3] University of Minnesota, Minneapolis, MN, USA*
*[4]University of California Davis, Davis, CA, USA*

## Abstract

Olivine lattice preferred orientation (LPO), or texture, forms in relation to deformation mechanisms such as dislocation creep and can be observed in the upper mantle as seismic anisotropy. Olivine is also mechanically anisotropic, meaning that it responds to stresses differently depending on the direction of the stress. Understanding the interplay between anisotropic viscosity (AV) and LPO, and their role in deformation, is necessary for relating seismic anisotropy to mantle flow patterns. In this study, we employ three methods to predict olivine texture (D-Rex, MDM, and MDM+AV) in a shear box model and a subduction model. D-Rex and MDM are two representative texture development methods that have been compared before, and our results are in line with previous studies showing that textures computed by D-Rex develop faster and are stronger and more point-like than textures calculated with MDM. MDM+AV uses the same no-AV mantle stresses and particle paths as D-Rex and MDM but includes the effect of AV for texture predictions. MDM+AV predicts a texture similar to MDM with a distinct girdle-like orientation in simple shear deformation or at low strain. At larger strains, MDM+AV's textures are more point-like and stronger compared to the other two methods. The effective viscosity for MDM+AV drops by up to 40% in

a shear box model, while the anisotropic viscosity can be both smaller and larger relative to the isotropic viscosity in different regions of a subduction model. Our results emphasize the significant role of AV in olivine texture development, which could substantially affect geodynamic processes in the upper mantle.

## 1. Introduction

Various geodynamic processes take place within Earth's upper mantle, such as subduction, seafloor spreading, lithospheric drips, and plumes, and have geological surface expressions such as tectonic plate movements, rifting, mountain building, volcanism, and dynamic topography. The physical and chemical properties of mantle materials control the deformation rates in the mantle associated with these processes. Understanding how minerals in the upper mantle respond to applied deformations is thus crucial for unraveling the mechanics of these geodynamic processes. Olivine, which constitutes approximately 60% of the upper mantle's composition, is the most abundant mineral, accompanied by pyroxene and other aluminous components. The olivine crystal structure has an orthorhombic crystal system characterized by three mutually perpendicular axes of different lengths (a ≡ [100], b ≡ [010], and c ≡ [001]). Slip primarily occurs on the (010) and (001) planes, with corresponding slip directions along [100] and [001] (Table 1 in Tommasi et al., 2000). Deformation processes in the upper mantle, such as dislocation creep and dynamic recrystallization on specific slip systems, lead to the development of lattice-preferred orientations (LPO), also known as crystal-preferred orientations (CPO), in olivine aggregates (Kaminski et al., 2004).

The internal crystallographic properties of olivine contribute significantly to macroscopic observations of seismic anisotropy. These properties are the primary source of seismic anisotropy in the upper mantle compared to extrinsic anisotropy resulting from mineral layering (Hansen et al., 2021). Seismic studies have revealed a velocity difference of up to 25% for P-wave velocity and 22% for S-wave velocity between olivine's fast and slow axes (Kumazawa, 1969). The widespread observations of seismic anisotropy around the world demonstrate that LPO is prevalent in the upper mantle (Long & Becker, 2010; Long & Silver, 2009). Therefore, investigating the microphysical mechanisms underlying seismic anisotropy in olivine is crucial for comprehending mantle dynamics and geodynamic processes.

Various numerical models have been developed to simulate olivine texture or LPO development and the resulting seismic anisotropy. These models can be categorized into three groups based on their assumptions: finite strain ellipsoid (FSE) models (McKenzie, 1979), polycrystal models (e.g., (Molinari et al., 1987; Ribe & Yu, 1991; Sarma & Dawson, 1996), and director method models (Muhlhaus et al., 2002). FSE-based models consider texture as independent of the deformation path, relying only on the total finite strain to compute the LPO evolution (McKenzie, 1979). Polycrystal models track individual grains and their contributions to the overall LPO, incorporating the effect of the initial texture and past deformation. VPSC (Tommasi et al., 2000) and D-Rex (Kaminski et al., 2004), two widely used models from this category, offer reasonable predictions of average LPO orientation and symmetry but require relatively high computational resources. Hansen et al. (2016b) demonstrated that these models predict both higher texture strength and larger anisotropy at high strains compared to other methods and experimental results. The director method, introduced by Muhlhaus et al. (2002), represents LPO using the orientation of the normal vectors of the anisotropy planes, called directors, which evolve based on the velocity gradient tensors. Hansen et al. (2016b) introduced the modified director method (MDM), which separately describes grain rotations and mechanical responses to address LPO development at high strains. MDM improves computational efficiency and prediction accuracy for larger strains and complicated deformation paths. This computational efficiency allowed Hansen et al. (2016b) to numerically optimize the parameters in this model to best reproduce LPOs observed in laboratory experiments. However, the application of MDM in subduction settings and other complex deformation scenarios remains unexplored.

Olivine also exhibits anisotropy in its mechanical properties, including viscosity, which significantly influences deformation rates and the resulting texture, ultimately impacting mantle flow dynamics by accelerating or decelerating mantle flow. Hansen et al. (2012) and Hansen et al. (2016a) conducted rock deformation experiments with olivine aggregates, and they demonstrated that the viscosity could change in response to the texture strength and orientation by approximately an order of magnitude, depending on the orientation of the principal stresses with respect to the texture alignment. While the above-mentioned texture evolution models have advanced our understanding of olivine LPO development, they have yet to incorporate the feedback effect of anisotropic viscosity (AV) on deformation. Previous numerical simulations demonstrated that AV can modify convection cells and patterns of the post-glacial rebound (Christensen, 1987; Han & Wahr, 1997), the temporal and spatial distributions of the Raleigh-Taylor instabilities (Lev & Hager, 2008), and the flow field and thermal structure within the mantle wedges of subduction systems (Lev & Hager, 2011).

More recent numerical modeling studies have shown that AV can significantly influence texture strength and orientation, leading to orders of magnitude changes in viscosity. Blackman et al. (2017) found that LPO and AV development creates a positive feedback in a mid-ocean ridge system, and the presence of AV significantly increases the calculated seismic anisotropy. Király et al. (2020) also predicted that olivine texture could weaken the asthenosphere and increase plate velocity by 60% if the plate movement is aligned with the preferred direction. However, further investigation is needed to compare different numerical methods for olivine texture computation and assess the effects of AV on texture predictions in both simple and complex settings.

This study aims to explore different olivine texture prediction methods in both simple and complex deformation settings by comparing the results from D-Rex, MDM, and MDM+AV. We use the deformation paths from numerical models run in the geodynamic modeling software ASPECT (Bangerth et al., 2020) to compute texture evolution for both D-REX, MDM, and MDM+AV. Additionally, MDM+AV represents viscosity with an anisotropic viscosity tensor instead of a scalar, allowing us to study the effect of AV on texture prediction. As a first step, this work focuses on the effects of AV on olivine texture and helps to determine whether implementing AV into future geodynamic modeling tools will significantly improve our understanding of geodynamic processes.

## 2. Methods

In this section, we present three distinct methods for the computation of olivine LPO development in both a simple-shear box configuration and a typical subduction configuration. While previous texture comparisons have centered on the differences between D-Rex and MDM in simple settings, we expand the comparison with a subduction model and the inclusion of AV in our third method. MDM+AV uses the same deformation history as D-Rex and MDM while incorporating AV in the texture prediction part. The details of each method and model setups are described below.

## 2.1. D-REX

D-Rex is a widely used polycrystal-type approach for predicting olivine texture evolution in aggregates subjected to large strains and high temperatures, particularly under intensive dynamic recrystallization (Kaminski & Ribe, 2001). It considers important factors such as the effect of initial LPO and deformation history, particularly relevant in the study of subduction systems where LPO can exhibit significant temporal and spatial variation. Compared to other polycrystal models like VPSC, D-Rex employs a simpler theory for olivine dynamic recrystallization and estimates dislocation density as a function of polycrystal orientation using only two free parameters. This simplification makes D-Rex less computationally intensive while still constrained by numerous experimental observations. Kaminski et al. (2004) expanded the model by incorporating the enstatite phase and-grain boundary migration into D-Rex.

In a recent work, Fraters & Billen (2021) implemented a version of D-Rex into the geodynamic modeling software ASPECT (Bangerth et al., 2020). ASPECT is an open-source, actively maintained geodynamic code integrated with Geodynamic World Builder (Fraters, 2020), which allows us to create realistic model setups such as the subduction model used in this study. Within ASPECT, D-Rex parameters are stored in particles, facilitating the tracking of olivine texture in regions of interest, such as around the subducting slab in the mantle. It is important to note that, in ASPECT, the volume fraction of the mineral phase m ($X_{\mathrm{m}}$) is removed from the definition of grain-boundary mobility ($M_{\mathrm{m}}$) as both parameters are treated independently. The D-Rex parameters that we can manipulate in ASPECT are grain-boundary mobility ($M_{\mathrm{m}}$), the threshold volume fraction for the activation of grain-boundary sliding ($f_{\mathrm{gbs}}$), and the nucleation rate ($\lambda$) (Kaminski et al., 2004). Boneh et al. (2015) found that their experimental data exhibited a better fit with D-Rex using $M_{\mathrm{m}} = 10$. Hansen et al. (2016b) also noted that D-Rex predictions with

$M_{\mathrm{m}} = 10$, $f_{\mathrm{gbs}} = 0.4$, and $\lambda = 5$ were most comparable to results obtained using MDM and their laboratory experiments.

### *2.2. MDM*

Muhlhaus et al. (2002) introduced the director method and represented the anisotropy of a material by the orientation of the directors, which are the normal vectors of the layered planes or slip surfaces. The directors can be advected with the velocity field and will rotate under deformation. The evolution of LPO can be computed based on the relationship between the current deformation field represented by the velocity gradient tensor and the orientation of the directors. Moreover, Muhlhaus et al. (2004) extended this method by incorporating temperature-dependent rheological parameters, demonstrating that the directors gradually align with the dominant flow direction or shear plane.

In a subsequent study, Hansen et al. (2016b) modified the original director method by redefining the director as the Burger's vector and defining the rotation rate to be dependent on both the Burger's vector and the slip plane. In this manner, the different olivine slip systems together control grain rotation (MDM). They calibrated $\tau_0$, the critical-resolved shear stress, and $f^{\alpha}$, the relative rotation rate of each slip system (denoted by $\alpha$) in the micromechanical and texture evolution model, respectively, using samples deformed under different paths (Hansen et al., 2016b). We used the same set of $\tau_0$ and $f^{\alpha}$ values for our MDM and MDM+AV models as defined in Hansen et al. (2016b).

### *2.3. MDM+AV*

To model texture evolution with the influence of AV, we combine the methods used by Király et al. (2020) and Signorelli et al. (2021). We first use the micromechanical model from Hansen et al. (2016b) to generate pairs of strain rates and stresses as input for the prediction. We then aim to find the set of Hill's coefficients (F, G, H, L, M, and N from Hill (1948)) that minimizes the difference between the norm of the input and the calculated strain rates ($\dot{\boldsymbol{\varepsilon}}$), defined by Signorelli et al. (2021) as:

$$\dot{\boldsymbol{\varepsilon}} = \gamma J\,(\sigma)^{\,n-1}\mathbf{A} : \mathbf{S}, \quad (1)$$

where

$\gamma = \gamma_0 \exp\left(\frac{-Q}{\mathrm{R}T}\right)$, with the experimentally derived fluidity ($\gamma_0$), the universal gas constant (R), and the temperature (*T*). $J\,(\sigma)$ is the equivalent stress defined by the Hill yield criteria (Hill, 1948):

$$J\,(\sigma) = (F(\sigma_{11} - \sigma_{22})^2 + G(\sigma_{22} - \sigma_{33})^2 + H(\sigma_{33} - \sigma_{11})^2 + 2L\sigma_{12}^2 + 2M\sigma_{23}^2 + 2N\,\sigma_{31}^2)^{1/2}. \quad (2)$$

**S** is the deviatoric stress tensor, *n* = 3.5 is the power-law exponent, and **A** is the non-dimensionalized anisotropic fluidity tensor:

$$\mathbf{A} = \frac{2}{3}\begin{bmatrix} F+H & -F & -H & 0 & 0 & 0 \\ -F & G+F & -G & 0 & 0 & 0 \\ -H & -G & H+G & 0 & 0 & 0 \\ 0 & 0 & 0 & L & 0 & 0 \\ 0 & 0 & 0 & 0 & M & 0 \\ 0 & 0 & 0 & 0 & 0 & N \end{bmatrix}, \quad (3)$$

Finally, with the best-fit Hill coefficients, we compute the fluidity tensor and predict a new strain rate using the stress tensor obtained from the geodynamic models in ASPECT (see below). Then the velocity gradient tensor obtained from ASPECT is scaled by the ratio between the components of the strain rate tensors from MDM+AV and the ASPECT model, and this new velocity gradient is used in the subsequent texture prediction. This representation of AV has yet to be implemented into the dynamic model, and with MDM+AV here, we will only look at how much AV could change the texture prediction part of the model, while the effect of AV on the velocity gradient tensor does not feed back to the geodynamic model evolution. It is also important to note that the calculation of the anisotropic fluidity tensor was performed in the LPO reference frame, and subsequently, we back-rotated the fluidity tensor to the model reference frame. The details of the rotation tensor formulation can be found in the supplementary information.

### *2.4. Model setup*

In this study, we conducted a comparative analysis of olivine textures predicted by D-Rex (calculated directly in ASPECT), MDM, and MDM+AV in both a shear box and a subduction setting. The initial Euler angles and strain rates on the particles from the ASPECT models were used as input for the MDM model to predict texture development under the same deformation conditions. Similarly, MDM+AV used the initial Euler angles, strain rates, stresses, and velocity gradients to compute texture, anisotropic viscosity, and a new strain rate.

The shear box is defined as a 1×1×1 $m^3$ cube in ASPECT, with a single particle consisting of 5000 olivine grains positioned at the center of the box, corresponding to the coordinate (0,0,0) (Figure 1). A velocity parallel to the x-direction and equal in magnitude to the z-coordinate is applied throughout the box, resulting in velocities of 0.5 m/s on the top and bottom faces of the box, pointing in opposite directions. Consequently, the second invariant of the strain-rate tensor ($\dot{\varepsilon}_{\mathrm{II}}$) at the particle is 0.5 $s^{-1}$. The shear box is deformed for 20 seconds under this velocity, and the total strain is thus 10. Subsequently, the applied strain rate and deformation tensors of the shear box are used as input for MDM and MDM+AV to calculate the texture evolution as defined above. The velocity gradient tensor is defined as follows:

$$D = \begin{bmatrix} 0 & 0 & 1 \\ 0 & 0 & 0 \\ 0 & 0 & 0 \end{bmatrix}. \qquad (4)$$

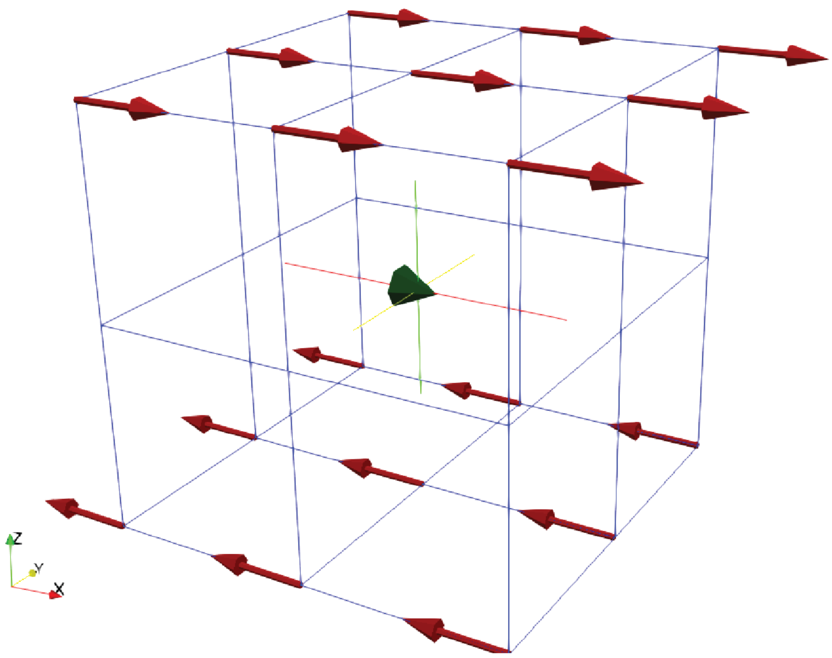


**Figure 1. Shear box model set-up and velocity boundary conditions. One particle with 5000 olivine grains sits in the center of the box to track the texture evolution.**

For the subduction model, we use the same settings as Fraters & Billen (2021) with a kinematically-driven subducting plate, and particles placed in particular to track the flow around the subducting plate. The domain is 2500×2000×800 $km^3$ in the x-, y-, and z-directions, respectively. Within the domain, an oceanic plate is pushed towards and subducted beneath a continental plate in the negative x-direction perpendicular to the plate boundary, with a dip angle of 50~55 degrees and a velocity of 3 cm/yr to initiate and drive subduction from the back of the subducting plate (Figure 2). The subduction trench spans 1000 km and is located 500 km from both sides of the model domain. Vertically, the model consists of a wet crust (30 km), a dry lithosphere (up to 100 km), and a wet upper mantle (up to 660 km) (Figure 2). The model includes two weak zones with an angle of internal friction of 5° and a cohesion of $1\times10^4$ Pa, lower than the surrounding lithosphere. The model employs free slip boundary conditions for its top surface and open boundary conditions on the east and west sides of the box.

We use incompressible viscoplastic rheology for the subduction model, and the viscosity is thus defined as:

$$\eta = \frac{1}{2} A^{-\frac{1}{n}} d^{\frac{m}{n}} \dot{\varepsilon}_{\mathrm{II}}^{\frac{1-n}{n}} \exp\left(\frac{E+PV}{n\mathrm{R}T}\right), (5)$$

where $A$ is the prefactor, $n$ is the stress exponent, $d$ is the grain size, $m$ is the grain-size exponent, $\dot{\varepsilon}_{\mathrm{II}}$ is the square root of the second invariant of deviatoric strain rate, $E$ is the activation energy, $P$ is the pressure, $V$ is the activation volume, R is the gas exponent, and $T$ is the temperature. We allow both dislocation creep and diffusion creep in our model; thus, the composite viscosity is defined as $\frac{\eta_{\mathrm{diff}} * \eta_{\mathrm{disl}}}{\eta_{\mathrm{diff}} + \eta_{\mathrm{disl}}}$. The values we use for the rheological behavior in the subduction model can be found in the supplementary information, and the parameter files are shared with Zenodo.

With the rheological behavior we described above using Eq. 5, the viscosity in the upper mantle is pressure dependent and will increase as the depth increases (Figure 2). We place 75 particles around the slab to study mantle flow on all sides of the slab and observe the deformation and texture tracked by these particles.

Most particles are located on the plane perpendicular to the y-axis at the center of the subducting plate in the sub-slab region and the mantle wedge region. In the results section, we examine two representative particles, one from the sub-slab area and one from the mantle wedge area, to demonstrate the spatial differences in deformation history for particles near a subduction zone.

For the MDM and MDM+AV texture simulations, we use the temperature, strain rate, velocity gradient, and stress that the particle experienced during the model run in ASPECT. In ASPECT, the subduction model has a composite rheological behavior with both dislocation creep and diffusion creep as mentioned above, while in the MDM+AV model, we assume that only dislocation creep gives rise to AV. We compute an effective viscosity for the MDM+AV model using the equivalent stress (from ASPECT) and strain rate (predicted using MDM+AV and eq. 1). To compare the change in viscosity under deformation with and without the effect of AV within MDM+AV, we also compute a predicted strain rate using an isotropic texture and an isotropic viscosity (IV) under this strain rate.

We compare the development of textures both quantitatively and qualitatively using texture scores representing the strength and shape of textures and pole figures of the distribution of the olivine a-axis representing the orientation of textures. The misorientation index (M-index) is defined as the difference between the observed misorientation angles and the misorientation angles for a uniform texture (Skemer et al., 2005). A minimum M-index score of 0 represents a uniform texture, and a maximum M-index score of 1 represents a strong single-crystal texture. To evaluate the shape of textures, we utilize the pointiness, girdle-ness, and randomness scores (P, G, and R scores) from Vollmer (1990). They represent components of a particular crystallographic

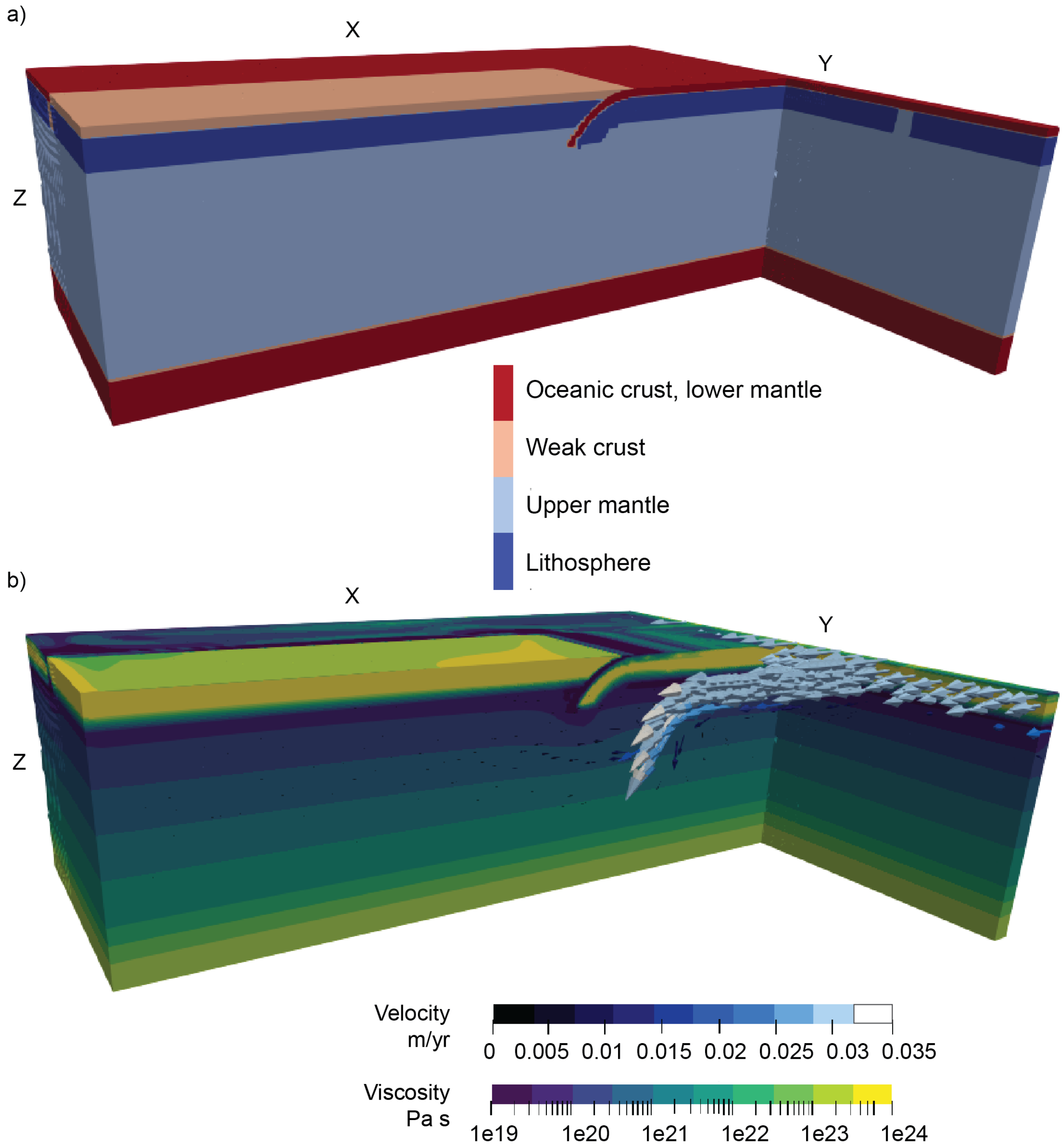


**Figure 2. a) Initial setup of the subduction model, showing a wet crust, a dry lithosphere, a wet upper mantle, and a wet lower mantle. b) A cross-section showing the viscosity on the cross-section with velocity vectors (on the middle cross-section and the subducting side) colored by their magnitudes.**

axis distribution derived from the eigenvalues of the orientation tensor for a single crystallographic axis. A high P, G, or R score corresponds to a point-like shape, a girdle-like single-plane shape, or a uniform texture, respectively. The P, G, and R scores add up to 1 and can be plotted on a ternary diagram.

# 3. Results

## *3.1. Shear box*

The particle undergoes a simple deformation path in the shear box setup with a constant strain rate and stress. In all three texture models, the particle starts with an isotropic texture and gradually reorients the a-axis direction into the shear direction as deformation accumulates. The girdle-ness score of the textures reaches its peak around an accumulated strain of 1 and starts decreasing, while the randomness score decreases from the initial value of 1 to less than 0.2 at an accumulated strain of 2 (Figure 3).

When comparing the texture evolution models, the alignment of the olivine a-axis with the shear direction in the D-Rex model occurs at a lower strain compared to the MDM and MDM+AV models. This distinction becomes visually evident in the pole figures (Figure 3a). The pointiness of a-axes and M-index scores exhibit a more rapid increase with increasing accumulated strain in D-Rex textures, in contrast with the MDM and MDM+AV textures (Figure 3b and c). During the early stage of deformation, the texture predicted by MDM and MDM+AV tends to organize into a girdle-like shape. Beyond this point, the girdle-ness score begins to decrease, and the pointiness score gradually catches up with the texture predicted by D-Rex. The girdle shape in the textures predicted by MDM and

MDM+AV persists until the end of the model, with a girdle-ness score of 0.23, in contrast to D-Rex, which shows no girdle shape with a girdle-ness score of 0.02. At an accumulated strain of 5, the M-index from D-Rex reaches its peak around 0.45 but starts to decrease and fluctuate ($0.41 \pm 0.02$) after that. In contrast, the M-index scores for both MDM and MDM+AV continues to increase monotonically, surpassing the M-index score for D-Rex after an accumulated strain of 8. Eventually, the textures predicted by all three methods converge with comparable pointiness scores (D-Rex: 0.734, MDM: 0.712, MDM+AV: 0.715) and M-index scores (D- Rex: 0.440, MDM: 0.439, MDM+AV: 0.445). Adding the AV component does not significantly change

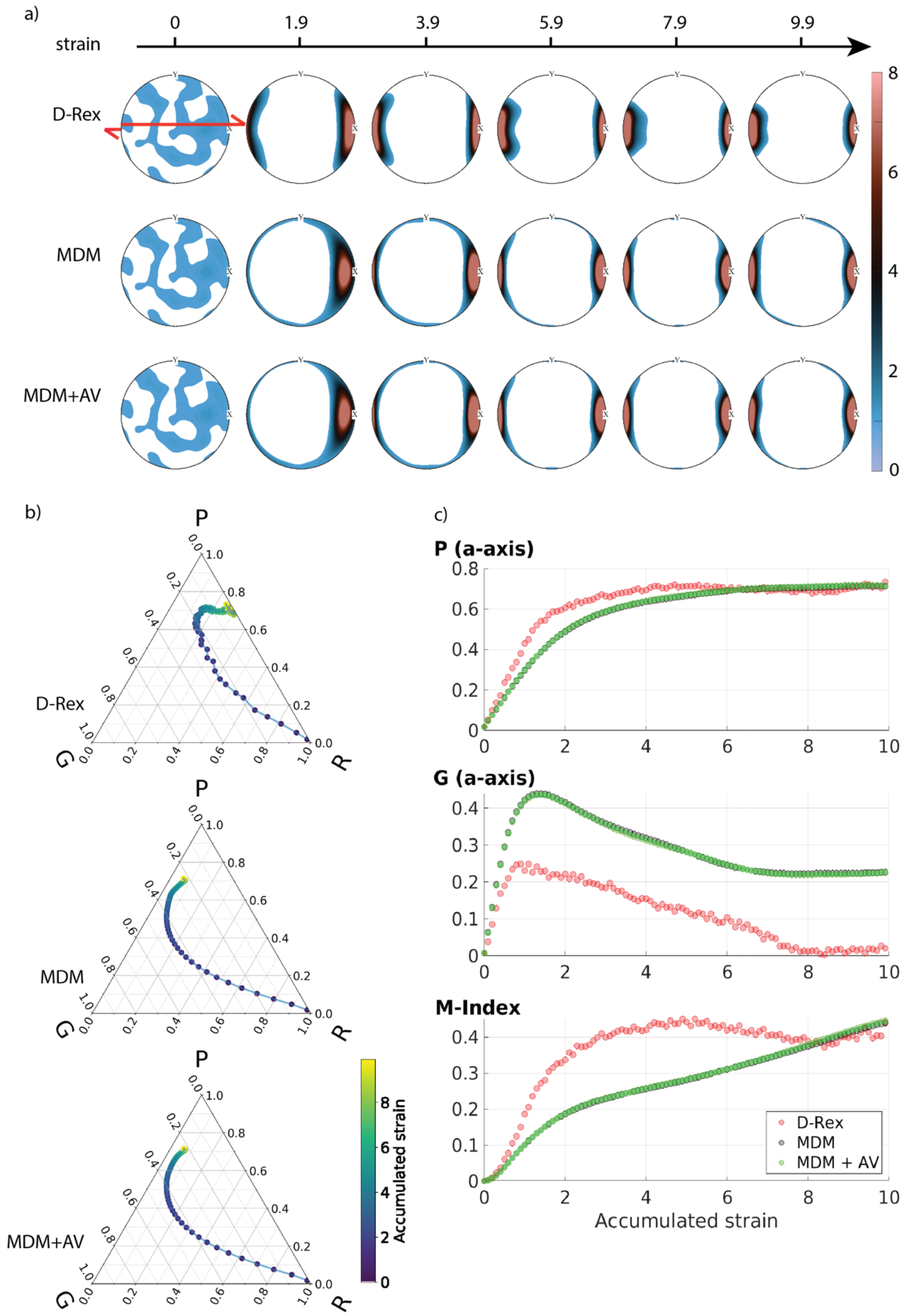


**Figure 3. a) Pole figures (upper hemisphere) illustrating the olivine particle's a-axis orientation in the shear box at different accumulated strains in the shear box model. Pole figures are contoured based on multiples of uniform distribution. The x, y directions are the same as in Figure 1. b) Ternary diagram plotting the pointiness, girdle-ness, and randomness (P, G, R) scores**

**of the olivine a-axis texture. The evolution of P, G, and R scores is colored by accumulated strain. c) Texture scores (pointiness, girdle-ness, and M-index) of the olivine particle in the shear box predicted by different methods.**

the texture predicted by MDM+AV, and it only increases the final M-index by less than 1% compared to D-Rex and MDM. When we examine the effective viscosity calculated from the equivalent stress and strain rate using the MDM+AV method, we observe that with this more aligned olivine texture, the effective viscosity decreases by 40% from the initial time step, which agrees with the results by Király et al. (2020).

### *3.2. Subduction*

Building upon our analysis of shear-box textures discussed earlier, we compare the texture predictions using similar criteria in a typical subduction setting. Figure 4 illustrates a sequence of snapshots captured at 10-Myr intervals of a cross-section in the middle of the subduction zone, showing viscosity (left) and strain rate (right) overlaid with velocity vectors represented by white arrows. The mantle wedge corner flow and the poloidal flow resulting from the slab's roll-forward motion are made evident by the velocity vectors (Figure 4). As subduction progresses, our trench gradually moves forward and has advanced approximately 100 km by the end of the model at 40 Myr (Figure 4e). Our analysis focuses on two particles representing distinct regions in a subduction zone: the sub-slab region (blue) and the mantle wedge region (pink). These particles experience different mantle flow patterns as the slab continues to subduct. The particle in the sub-slab region is located about 100 km beneath the lithosphere, moving with the mantle flow behind the subducting slab forwards and downwards simultaneously. The particle in the mantle wedge follows the corner flow upwards and towards the slab until about 5 Myr. Then it gets near the slab with its temperature dropping from around 1535 K to below 1400 K and starts to move downwards together with the slab.

For the sub-slab particle, our results show that both MDM and MDM+AV predict a similar texture evolution, characterized by a more girdle-like shape of the a-axis distribution compared to D-Rex's prediction, which transitions into a more point-like shape at around a strain of 0.8 (Figure 5). This behavior is consistent with the observation made in the shear-box experiment. D-Rex predicts a shift from a point-like to a more random texture after an accumulated strain of 1, while both MDM and MDM+AV predict a steady increase in the pointiness score. Additionally, around an accumulated strain of 0.8, the girdle-ness of the texture from MDM+AV reaches its peak of 0.33 and then starts to decrease slowly, while the pointiness score continues to increase, becoming the highest among the three methods (Figure 5c). As the texture develops in this particle, the effective

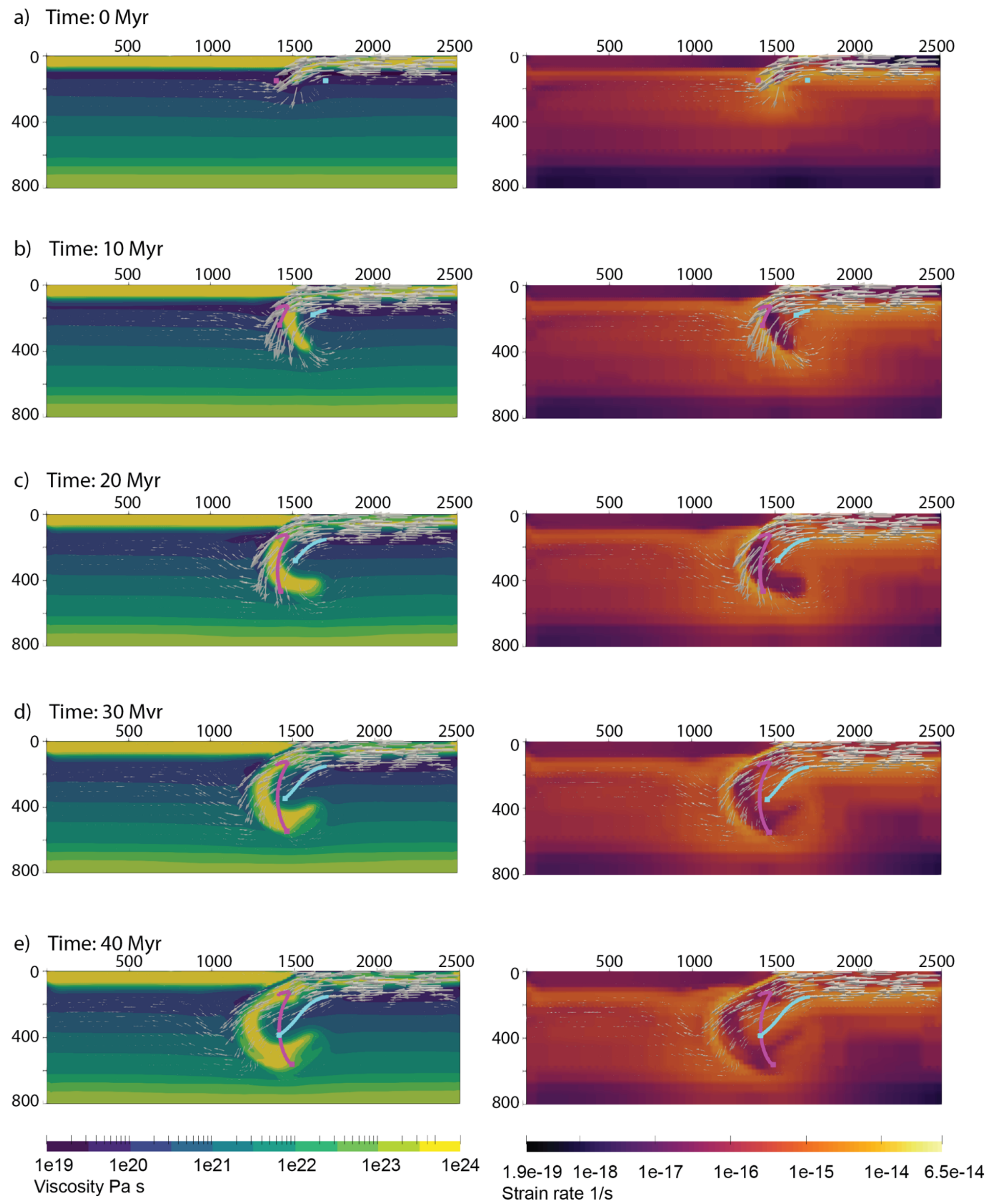


**Figure 4. Slice in the middle of the subduction model (ASPECT with texture model D-Rex), displaying the viscosity (left column) and strain rate (right column) represented by the background color, velocity represented by the white arrows above the background, and the two particles of interest represented by spheres (blue: sub-slab particle, pink: mantle-wedge particle). The movement of the particles is captured in five snapshots (0 Myr, 10 Myr, 20 Myr, 30 Myr, and 40 Myr) during the model. MDM and MDM+AV**

**use the particle deformation paths from this model. The horizontal axis is the x-axis, and the vertical axis is the z-axis.**

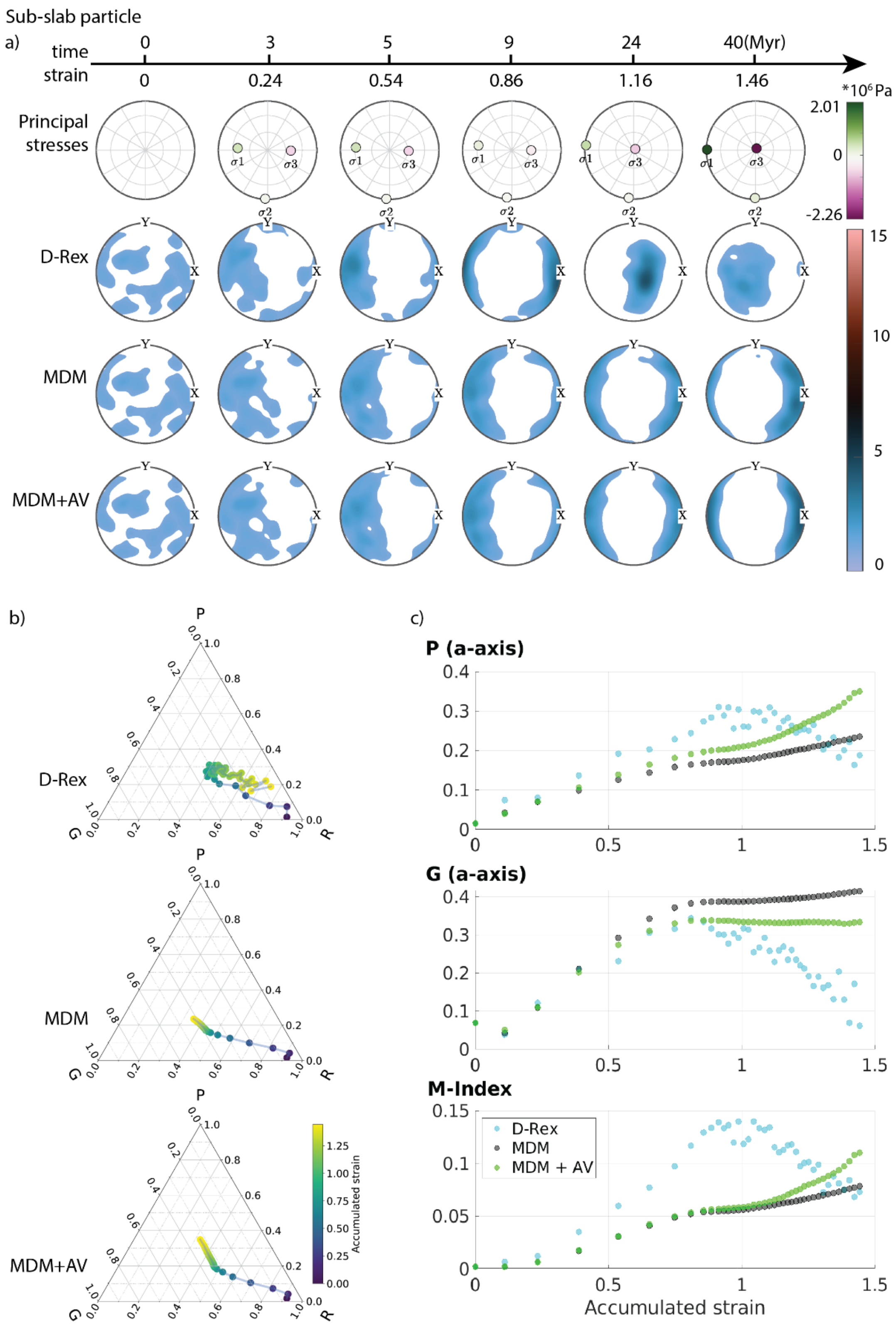


**Figure 5. a) Principal stresses of the deviatoric stress tensor and pole figures (upper hemisphere) of an olivine particle from the sub-slab area of the subduction model at selected accumulated strains. The particle's location can be found in Figure 4 (blue). The orientations of the x, y, and z-axis in these pole figures are the same as in Figures 2 and 4, so the xy-plane here is the horizontal plane in Figure 2 as viewed from the top of the model. The**

**orientations of the principal stresses are also indicated for each selected strain. We follow the convention of positive tensional stress. b) Ternary diagram of the particle's P, G, and R scores from the sub-slab area of the subduction model. c) Texture scores (P, G scores, and M-index) of the olivine particle from the sub-slab area of the subduction model.**

viscosity from MDM+AV (AV) becomes increasingly weaker than the effective viscosity from an isotropic texture (IV), as defined above in the method section (Figure 6a). The AV decreases from 100% to about 80% of the IV during the formation of the girdle plane. Then the AV-to-IV ratio remains stable until the pointiness score approaches the girdle-ness score and the point-like shape gains dominance in the texture. There is a tendency of a 30% weakening in the AV towards the end of the model. To help understand the evolution of the effective viscosity for MDM+AV, we plot the orientations of the principal stresses from the deviatoric stress tensor derived from the subduction model in ASPECT above the texture plots (Figure 5a). The significant increase in the magnitude of the largest principal stress ($\sigma 1$) coincides with the drop in the effective viscosity for both AV and IV (Figure 6a), consistent with the shear-thinning nature of the power law in Eq. 1. The slight misalignment of $\sigma 1$ with the direction of the *a*-axis point maximum correlates with the weakening of AV relative to IV. This relative decrease in AV also correlates with the increasing pointiness score (Figure 5 and 6a). The total accumulated strain for this particle is around 1.5, and the texture predicted by all three methods is not very strong.

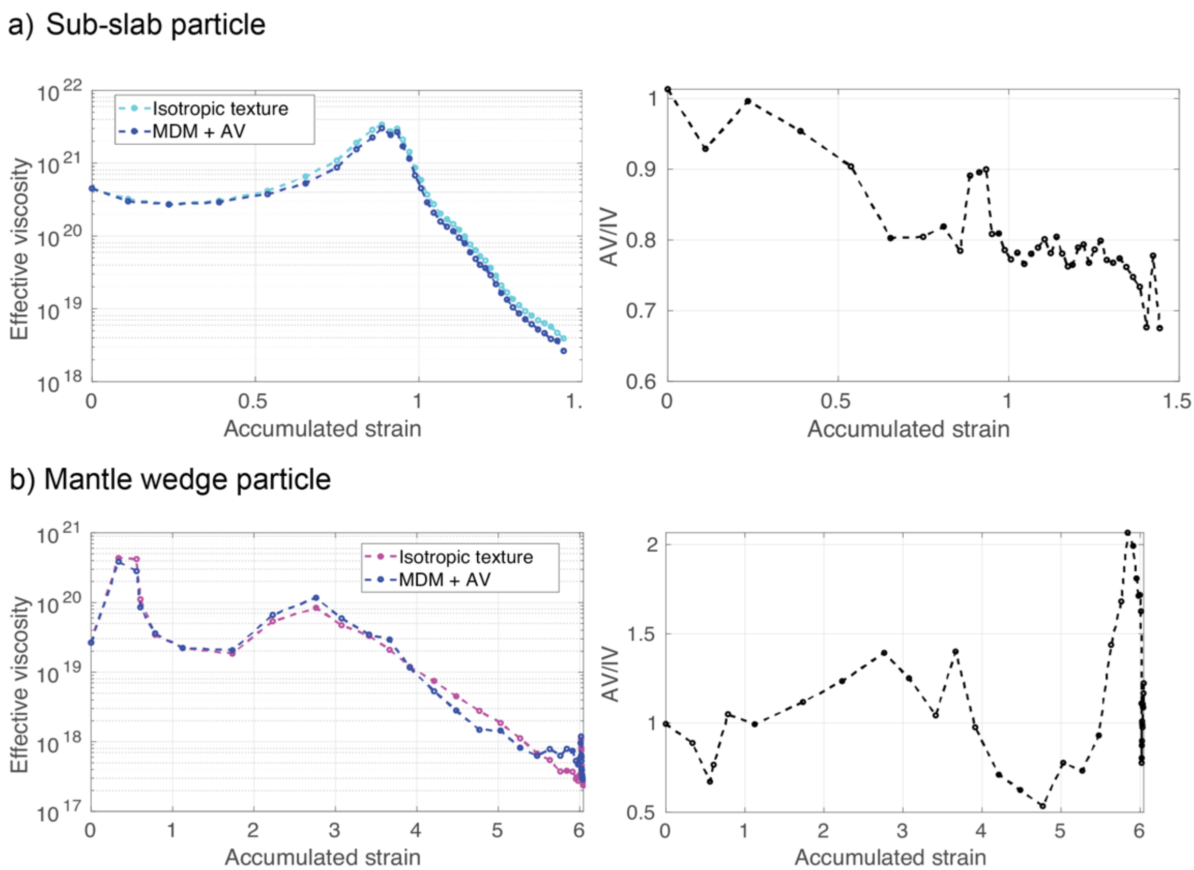


**Figure 6. a) Effective viscosity from MDM+AV and from using a random, isotropic texture (left) and the ratio between these viscosities (right) for the sub-slab particle. b) The same plots for the olivine particle from the mantle wedge area in the subduction model.**

For the particle in the mantle wedge region, our analysis reveals that MDM+AV predicts a more point-like texture (MDM+AV pointiness score = 0.65), distinct from the strong girdle-like texture predicted by MDM (MDM girdle-ness score = 0.56) and the weaker point-like texture by D-Rex (D-Rex pointiness score = 0.45) (Figure 7). Still, D-Rex is the fastest to develop a point-like feature in the texture, while the MDM texture tends to organize into a girdle plane. In the MDM+AV model, the texture is similar to MDM until an accumulated strain of 5, at which point the point-like feature replaces the girdle-like feature, and consequently, the pointiness score predicted by MDM+AV reaches the largest of all at the end of the model. Initially, AV is weaker than IV during the formation of the girdle plane, on which the principal stress direction lies (Figure 6b and Figure 7a). As the principal stresses rotate away from the girdle plane in the texture, the AV of the particle is hardened to about 1.5 times the IV. Gradually, the a-axis maximum rotates to bisect $\sigma_1$ and $\sigma_3$ at a strain of ~4, associated with a decrease of the AV to 50% of the IV. Towards the end of the simulation, both $\sigma_1$ and $\sigma_3$ become perpendicular to the developing point maximum within the texture, and this particle experiences a hardening effect in AV, reaching up to about 200% of IV (Figure 6b).

## 4. Discussion

The findings presented in the results section provide valuable insights into the implications of different texture evolution methods and the role of anisotropic viscosity (AV) within both simple shear and subduction systems. In the context of simple deformation settings, such as in a shear box model, our study reveals that the olivine texture predicted by the D-Rex method aligns more rapidly with the shear direction compared to the texture predicted by the MDM, which is consistent with previous modeling outcomes from Hansen et al. (2016b). As strain accumulates, textures predicted by all three methods reach similar pointiness and M-index scores, eventually aligning with the shear direction under large strain. The main distinction between the MDM and the D-Rex textures lies in the girdle-ness scores. While the random texture starts to organize into a point-like shape in the D-Rex model, a girdle is forming in the MDM model, and the girdle-ness score for MDM remains larger than the girdle-ness score for the D-Rex model at the end of the experiment. The presence of a girdle shape in the texture predicted from MDM has also been observed by Hansen et al. (2016b). The effect of AV is not significant for the texture shape, strength, and

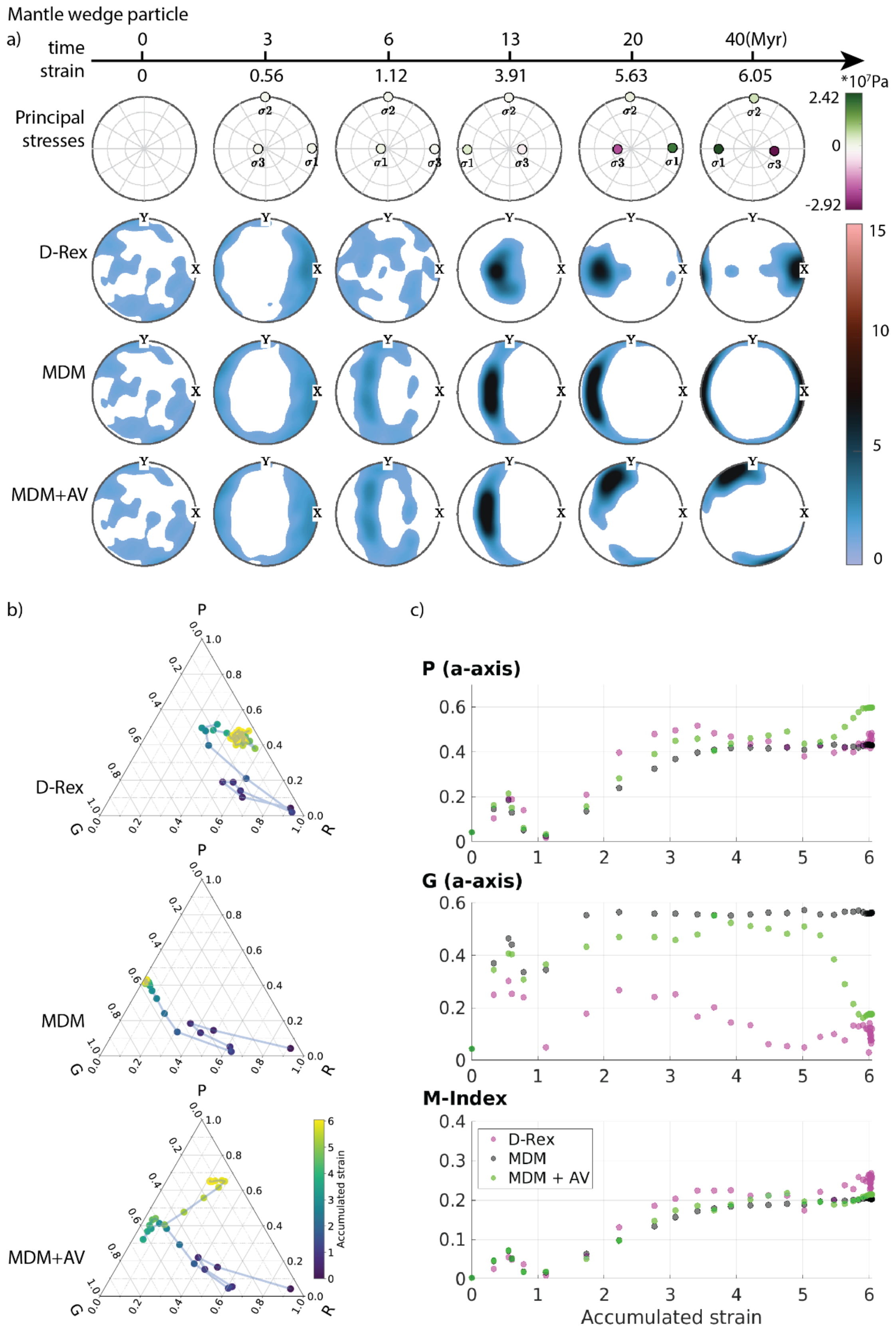


**Figure 7. a) Principal stresses of the deviatoric stress tensor and pole figures (upper hemisphere) of an olivine particle from the mantle wedge area of the subduction model at selected accumulated strains. The particle's location can be found in Figure 4 (pink). b) Ternary diagram of the P, G, and R scores**

**of the olivine particle from the sub-slab area of the subduction model. c) Texture scores (P, G scores, and M-index) of the olivine particle from the sub-slab area of the subduction model.**

orientation within the shear box model, as the texture scores of MDM+AV differ by less than 1% from the scores of MDM and D-Rex textures. In the shear box model, we observe an inverse correlation between the decreasing effective viscosity and the increasing pointiness score of the olivine a-axis. As was demonstrated by Király et al. (2020), the effective viscosity decreases by about 40% as the pointiness of the texture increases in the model with AV, leading to a substantial amount of weakening. Overall, we find that adding AV does not change the texture significantly. This aligns with our expectation, given that the shear box model has a simple and homogeneous set-up, and the boundary conditions are imposed such that the variation in viscosity cannot change the imposed strain rate. Using the MDM+AV predicted strain rate in the dynamic model and allowing AV to change the deformation paths could amplify the effect of AV. Since D-Rex textures align to the shear direction faster and the effective viscosity anticorrelates with the pointiness score, we expect a stronger anisotropy and more weakening if we implement AV with D-Rex textures (as in ASPECT).

By examining the particles from the sub-slab and mantle-wedge regions of a trench-advance subduction model, we observe distinct texture evolutions showing more differences among the MDM+AV, MDM, and D-Rex methods. The amount of deformation and strain rate differ across particles, with sub-slab particles experiencing less deformation (~1 accumulated strain) compared to mantle wedge particles (~6 accumulated strain) over 40 Myrs of simulation. This difference agrees with the roll-forward geometry and the mobility of the trench in our subduction model. The resulting texture strength correlates with the intensity of deformation, where particles experiencing substantial deformation tend to have a stronger texture, characterized by higher texture scores. It is worth noting that the amount of deformation from the subduction model is not very large due to the limited lateral motion of the trench. We expect more deformation in a trench-retreating subduction model or with pre-existing texture and, thus, a larger anisotropy.

Although the amount of deformation is different, for both particles we studied in the subduction model, the girdle-like feature still exists in the texture predicted by MDM and is much stronger compared to the girdle-ness of D-Rex textures, consistent with the observations from the shear box experiments. The pointiness of the D-Rex texture in the sub-slab particle is not significant at an accumulated strain of 1.5; however, at a larger strain (~6), the pointiness of the mantle wedge particle is around twice as large. MDM+AV initially predicts a texture evolution trend similar to MDM for both particles. Nevertheless, as the initial girdle-like shape quickly shifts to a point maximum in the D-Rex texture, the point-like shape also dominates the MDM+AV texture and leads to its highest pointiness score among the three methods. In addition, for the mantle wedge particle, adding AV induces a rotation of the point maximum into the y-direction, forming a texture that, if AV were implemented in the flow calculation, could change the particle path. This is due to the enhancement of the velocity gradient into the y-direction due to AV rheology. See part 3 in the Supplementary Information.

For both particles during the ASPECT model run, the dislocation creep mechanism dominates most of the modeled time ($\frac{\eta_{dislocation}}{\eta_{diffusion}} < 1$). This observation means that using a rheological model consisting only of power-law dislocation creep in MDM+AV remains a valid representation of the impact of AV. By plotting the principal stress directions at different strain stages, we observe that both particles experience a significant increase in the principal stresses, especially $\sigma_3$, the compressive stress, as the sub-slab particle is pushed by the rolling slab, and the mantle wedge particle is pushed by the slab tip and the lower boundary. The weakening effect of AV, signaled by an AV-to-IV ratio smaller than 1, tends to coincide with the maximum a-axis direction being at an angle to both $\sigma_1$ and $\sigma_3$ (Figure 5 and 7). The largest weakening effect occurs when the a-axis maximum bisects $\sigma_1$ and $\sigma_3$, which is observed at a strain of ~4 for the mantle-wedge particle (Figure 7a). That is, when the a-axis maximum is aligned with the direction of maximum shear stress. This observation is consistent with the maximum shear stress being well resolved on the two weakest slip systems, (010)[100] and (001)[100]. For the sub-slab particle, the MDM+AV effective viscosity is smaller than the isotropic viscosity throughout the model run, and AV could be weakened to about 70% of IV. The effect of AV is larger and more complex for the particle in the mantle wedge region, which experiences both weakening ($\frac{AV}{IV} \sim 50\%$) and hardening ($\frac{AV}{IV} \sim 200\%$) effects of AV depending on the relationship between the texture and the stress conditions. This is because the accumulated strain in the mantle wedge is larger, leading to a stronger texture and anisotropy, while the stress on the particle is changing. Such a weakening or hardening effect would modify the deformation path of the particle and the mantle flow patterns for a subduction setting. To fully comprehend the effect of AV in a subduction zone, it is necessary to implement AV rheology into geodynamic modeling software like ASPECT, which would allow us to study the modified mantle deformation.

These findings are consistent with previous knowledge and demonstrate that the effect of AV is significant and should be included in geodynamic models. When the direction of maximum shear stress aligns with the dominant a-axis orientation, the anisotropy of viscosity weakens the material significantly. On the other hand, if the direction of maximum shear stress is perpendicular to the strong a-axis alignment as at the end of the MDM+AV model for the mantle wedge particle, the material will be hardened. Our study offers the first step towards incorporating AV into numerical methods and an application of MDM+AV to reproduce the effect of AV in both simple and complex scenarios. If we assume that the shear direction is the same as the texture alignment, the deformation needed to produce such texture interpreted from seismic anisotropy is smaller with the effect of AV than for an isotropic material. However, the scope of this study is limited to textures tracked by a few particles within a specific subduction model. Further investigation should encompass different regions within a subduction zone to examine the spatial and temporal variations of the relationship between deformation and AV. Additionally, running models with diverse subduction settings, such as subduction with a retreating trench, oblique subduction, and flat subduction, will further enhance our understanding of the importance of AV and rock texture within subduction zones. To comprehensively explore this representation of AV, it is also crucial to run models that accurately represent specific subduction zones, compute seismic anisotropy, and compare the results with observations.

## 5. Conclusion

Our study explores olivine texture evolution in both a simple shear box setting and a typical subduction setting using three different methods, D-Rex, MDM, and MDM+AV. The results are consistent with previous modeling and experimental results and show that the D-Rex texture is usually stronger and has a point-like shape. In contrast, the MDM texture develops more slowly and has more of a girdle-like shape. The resulting effective viscosity for MDM+AV could weaken by about 40% in the shear box model. It could be weakened or hardened in different regions in the subduction model. The effect of AV may be reduced if we incorporate multiple deformation mechanisms acting together to accommodate the strain, which might reduce the impact of the anisotropic component. In the future our aim is to implement AV into ASPECT, where anisotropic viscosity would be (initially) coupled with D-REX. Since D-Rex predicts a stronger and more point-like texture alignment, this implementation could lead to an overprediction of the weakening effect of AV with respect to the simple models using MDM+AV (e.g. in Király et al. (2020)) for textures in which the LPO aligns with the main shear direction. Our results suggest that the AV of olivine greatly impacts texture formation and the rheology in the upper mantle. Hence AV could significantly affect geodynamic processes in the upper mantle such as subduction where deformation by dislocation creep dominates under various circumstances. Furthermore, due to its effect on texture formation, counting with AV in subduction models can significantly improve our interpretations of seismic anisotropy observations.

**Acknowledgments**

This research was supported by the Research Council of Norway's project 314742 (ANIMA) and its Centers of Excellence projects 223272 (CEED) and 332523 (PHAB).

**Author contributions**

Y. Wang wrote the original draft, conducted analysis, and made figures under the supervision of Á. Király and C. P. Conrad. L. Hansen provided the original MDM method, and M. Fraters provided the original model parameter file. All authors contributed to the reviewing and editing of this article.

## Data availability

The version of modeling software ASPECT used in this project is based on ASPECT 2.2.0 (Bangerth et al., 2022) and the CPO implementation from (Fraters & Billen, 2021) with additional changes not merged to the main repository. It is available through GitHub (https://github.com/Wang-yijun/aspect/tree/LPO_ss_tensor) and zenodo (DOI:10.5281/zenodo.8219018). Predictions of MDM and MDM+AV textures, comparisons of the textures, and analysis are generated with MATLAB and Python scripts available through Zenodo (DOI:10.5281/zenodo.8247969).

## References

Bangerth, W., Dannberg, J., Fraters, M., Gassmoeller, R., Glerum, A., Heister, T., Myhill, R., & Naliboff, J. (2022). *ASPECT v2.4.0* [Computer software]. Zenodo. https://doi.org/10.5281/zenodo.6903424

Bangerth, W., Dannberg, J., Gassmoeller, R., & Heister, T. (2020). *ASPECT v2.2.0* [Computer software]. Zenodo. https://doi.org/10.5281/zenodo.3924604

Blackman, D. K., Boyce, D. E., Castelnau, O., Dawson, P. R., & Laske, G. (2017). Effects of crystal preferred orientation on upper-mantle flow near plate boundaries: Rheologic feedbacks and seismic anisotropy. *Geophysical Journal International*, *210*(3), 1481–1493. https://doi.org/10.1093/gji/ggx251

Boneh, Y., Morales, L. F. G., Kaminski, E., & Skemer, P. (2015). Modeling olivine CPO evolution with complex deformation histories: Implications for the interpretation of seismic anisotropy in the mantle. *Geochemistry, Geophysics, Geosystems*, *16*(10), 3436–3455. https://doi.org/10.1002/2015GC005964

Christensen, U. R. (1987). Some geodynamical effects of anisotropic viscosity. *Geophysical Journal of the Royal Astronomical Society*, *91*(3), 711–736. https://doi.org/10.1111/j.1365-246X.1987.tb01666.x

Fraters, M. (2020). *The Geodynamic World Builder* [Computer software]. Zenodo. https://doi.org/10.5281/zenodo.3900603

Fraters, M. R. T., & Billen, M. I. (2021). On the Implementation and Usability of Crystal Preferred Orientation Evolution in Geodynamic Modeling. *Geochemistry, Geophysics, Geosystems*, *22*(10). https://doi.org/10.1029/2021GC009846

Han, D., & Wahr, J. (1997). An analysis of anisotropic mantle viscosity, and its possible effects on post-glacial rebound. *Physics of the Earth and Planetary Interiors*, *102*(1), 33–50. https://doi.org/10.1016/S0031-9201(96)03268-2

Hansen, L. N., Conrad, C. P., Boneh, Y., Skemer, P., Warren, J. M., & Kohlstedt, D. L. (2016). Viscous anisotropy of textured olivine aggregates: 2. Micromechanical model. *Journal of Geophysical Research: Solid Earth*, *121*(10), 7137–7160. https://doi.org/10.1002/2016JB013240

Hansen, L. N., Faccenda, M., & Warren, J. M. (2021). A review of mechanisms generating seismic anisotropy in the upper mantle. *Physics of the Earth and Planetary Interiors*, *313*, 106662. https://doi.org/10.1016/j.pepi.2021.106662

Hansen, L. N., Warren, J. M., Zimmerman, M. E., & Kohlstedt, D. L. (2016). Viscous anisotropy of textured olivine aggregates, Part 1: Measurement of the magnitude and evolution of anisotropy. *Earth and Planetary Science Letters*, *445*, 92–103. https://doi.org/10.1016/j.epsl.2016.04.008

Hansen, L. N., Zimmerman, M. E., & Kohlstedt, D. L. (2012). Laboratory measurements of the viscous anisotropy of olivine aggregates. *Nature*, *492*(7429), 415–418. https://doi.org/10.1038/nature11671

Hill, R. (1948). A theory of the yielding and plastic flow of anisotropic metals. *Proceedings of the Royal Society of London. Series A. Mathematical and Physical Sciences*, *193*(1033), 281–297. https://doi.org/10.1098/rspa.1948.0045

Kaminski, É., & Ribe, N. M. (2001). A kinematic model for recrystallization and texture development in olivine polycrystals. *Earth and Planetary Science Letters*, *189*(3–4), 253–267. https://doi.org/10.1016/S0012-821X(01)00356-9

Kaminski, É., Ribe, N. M., & Browaeys, J. T. (2004). D-Rex, a program for calculation of seismic anisotropy due to crystal lattice preferred orientation in the convective upper mantle. *Geophysical Journal International*, *158*(2), 744–752. https://doi.org/10.1111/j.1365-246X.2004.02308.x

Király, Á., Conrad, C. P., & Hansen, L. N. (2020). Evolving Viscous Anisotropy in the Upper Mantle and Its Geodynamic Implications. *Geochemistry, Geophysics, Geosystems*, *21*(10). https://doi.org/10.1029/2020GC009159

Kumazawa, M. (1969). The elastic constants of single-crystal orthopyroxene. *Journal of Geophysical Research (1896-1977)*, *74*(25), 5973–5980. https://doi.org/10.1029/JB074i025p05973

Lev, E., & Hager, B. H. (2008). Rayleigh-Taylor instabilities with anisotropic lithospheric viscosity. *Geophysical Journal International*, *173*(3), 806–814. https://doi.org/10.1111/j.1365-246X.2008.03731.x

Lev, E., & Hager, B. H. (2011). Anisotropic viscosity changes subduction zone thermal structure: ANISOTROPIC VISCOSITY CHANGES WEDGE THERMAL

STRUCTURE. *Geochemistry, Geophysics, Geosystems*, *12*(4), n/a-n/a. https://doi.org/10.1029/2010GC003382

Long, M. D., & Becker, T. W. (2010). Mantle dynamics and seismic anisotropy. *Earth and Planetary Science Letters*, *297*(3), 341–354. https://doi.org/10.1016/j.epsl.2010.06.036

Long, M. D., & Silver, P. G. (2009). Shear Wave Splitting and Mantle Anisotropy: Measurements, Interpretations, and New Directions. *Surveys in Geophysics*, *30*(4), 407–461. https://doi.org/10.1007/s10712-009-9075-1

McKenzie, D. (1979). Finite deformation during fluid flow. *Geophysical Journal International*, *58*(3), 689–715. https://doi.org/10.1111/j.1365-246X.1979.tb04803.x

Molinari, A., Canova, G. R., & Ahzi, S. (1987). A self consistent approach of the large deformation polycrystal viscoplasticity. *Acta Metallurgica*, *35*(12), 2983–2994. https://doi.org/10.1016/0001-6160(87)90297-5

Muhlhaus, H.-B., Moresi, L., & Cada, M. (2004). Emergent Anisotropy and Flow Alignment in Viscous Rock. *Pure and Applied Geophysics*, *161*(11–12). https://doi.org/10.1007/s00024-004-2575-5

Muhlhaus, H.-B., Moresi, L., Hobbs, B., & Dufour, F. D. R. (2002). Large Amplitude Folding in Finely Layered Viscoelastic Rock Structures. *Pure Appl. Geophys.*, *159*.

Ribe, N. M., & Yu, Y. (1991). A theory for plastic deformation and textural evolution of olivine polycrystals. *Journal of Geophysical Research: Solid Earth*, *96*(B5), 8325–8335. https://doi.org/10.1029/90JB02721

Sarma, G. B., & Dawson, P. R. (1996). Effects of interactions among crystals on the inhomogeneous deformations of polycrystals. *Acta Materialia*, *44*(5), 1937–1953. https://doi.org/10.1016/1359-6454(95)00309-6

Signorelli, J., Hassani, R., Tommasi, A., & Mameri, L. (2021). An effective parameterization of texture-induced viscous anisotropy in orthotropic materials with application for modeling geodynamical flows. *Journal of Theoretical, Computational and Applied Mechanics*, 6737. https://doi.org/10.46298/jtcam.6737

Skemer, P., Katayama, I., Jiang, Z., & Karato, S. (2005). The misorientation index: Development of a new method for calculating the strength of lattice-preferred orientation. *Tectonophysics*, *411*(1–4), 157–167. https://doi.org/10.1016/j.tecto.2005.08.023

Tommasi, A., Mainprice, D., Canova, G., & Chastel, Y. (2000). Viscoplastic self-consistent and equilibrium-based modeling of olivine lattice preferred orientations: Implications for the upper mantle seismic anisotropy. *Journal of Geophysical Research*, *105*, 7893–7908. https://doi.org/10.1029/1999JB900411

Vollmer, F. W. (1990). An application of eigenvalue methods to structural domain analysis. *Geological Society of America Bulletin*, *102*(6), 786–791. https://doi.org/10.1130/0016-7606(1990)102<0786:AAOEMT>2.3.CO;2

Supplementary Information

Table of contents



# 1. Rheology parameters

$$\eta_i = \frac{1}{2} A_i^{-\frac{1}{n_i}} d^{\frac{m_i}{n_i}} \dot{\varepsilon}_{ii}^{\frac{1-n_i}{n_i}} exp\left(\frac{E_i + PV_i}{nRT}\right)$$

$$\eta = \frac{\eta_{diff} * \eta_{disl}}{\eta_{diff} + \eta_{disl}}$$

Table 1 – Rheology parameters of the subduction model.

| | Overriding crust | Continental crust | Weak crust | Weak lithosphere | Upper mantle | Lower mantle |
|---|---|---|---|---|---|---|
| $A_{disl}(Pa^{-n}s^{-1})$ | 8.57e-28 | 8.57e-28 | 8.57e-28 | 6.51e-15 | 6.51e-15 | 6.51e-16 |
| $n_{disl}$ | 4 | 4 | 4 | 3.8 | 3.5 | 3.5 |
| $E_{disl}\ (kJ/mol)$ | 223 | 223 | 223 | 440 | 530 | 530 |
| $V_{disl}(m^3/mol)$ | 18e-6 | 18e-6 | 18e-6 | 18e-6 | 18e-6 | 18e-6 |
| $A_{diff}(m^m/Pas)$ | 8.88e-15 | 8.88e-15 | 8.88e-15 | 8.88e-15 | 8.88e-15 | 8.88e-15 |
| $E_{diff}\ (kJmol^{-1})$ | 375 | 375 | 375 | 335 | 335 | 355 |
| $V_{diff}(m^3/mol)$ | 6e-6 | 6e-6 | 6e-6 | 6e-6 | 6e-6 | |
| Angle of internal friction (°) | 10 | 1 | 5 | 10 | 15 | 15 |
| Cohesion (Pa) | 10e6 | 1e4 | 1e4 | 10e6 | 20e6 | 20e6 |
| Density $(kg/m^3)$ | 3300 | 3399 | 3300 | 3200 | 3200 | 3200 |

# 2. Rotation from the model reference frame to CPO reference frame and back

The constitutive equation that relates stress and strain rate utilizes a fourth-rank anisotropic viscosity tensor such that: $\sigma_{kl} = \eta_{ijkl} * \dot{\varepsilon}_{ij}$. Here the viscosity tensor $\eta_{ijkl}$ has 81 independent components. For an olivine aggregate we can assume monoclinic symmetry, meaning that $\eta_{ijkl}$ for olivine has 21 independent components in our model reference frame. To use Hill's parameters for the anisotropic viscosity tensor (Signorelli et al., 2021),we need to rotate to the mean CPO reference frame where we can assume an orthotropic symmetry.

To compute the rotation matrix ($R_{CPO}$) between the model and the CPO reference frame, we first compute the mean orientation of the a-, b-, and c- axes of olivine by taking the eigenvalues and eigenvectors of the orientation matrices for each axis. This method is equivalent to the Bingham average computation as in ASPECT described by Fraters and Billen (2021). We construct $R_{CPO}$ from the eigenvectors with the largest associated eigenvalues for each axis and now we have:

$$R_{CPO} = \begin{bmatrix} \max\_eigenvector\_a(1) & \max\_eigenvector\_b(1) & \max\_eigenvector\_c(1) \\ \max\_eigenvector\_a(2) & \max\_eigenvector\_b(2) & \max\_eigenvector\_c(2) \\ \max\_eigenvector\_a(3) & \max\_eigenvector\_b(3) & \max\_eigenvector\_c(3) \end{bmatrix}$$

The constitutive equation (equation 9) from Signorelli et al. (2021) in the CPO reference frame is:

$\dot{\varepsilon}_{CPO} \ = \ \gamma \, \mathrm{J} \, (\sigma_{CPO})^{\,n-1} \mathrm{A} : (R'_{CPO} \colon \sigma_{mod} \colon R_{CPO}),$

where $\sigma_{mod}$ is the stress in model reference frame. To find the strain rate in model reference frame, we first need to rotate the stress in model reference frame into the CPO reference frame in order to calculate anisotropic viscosity tensor. Then we rotate the fluidity tensor back into model reference frame. Thus, the constitutive equation that we use in model reference frame is:

$$\dot{\varepsilon}_{mod} \ = (R_{CPO\_K} \colon (\gamma \, \mathrm{J} \, (R'_{CPO} \colon \sigma_{mod} \colon R_{CPO})^{n-1} \mathrm{A}) \colon R'_{CPO\_K}) \colon \sigma_{mod}$$

where $R_{CPO\_K}$ is the rotation matrix that rotates the fourth-rank tensor in Kelvin notation from the CPO reference frame to model reference frame constructed from $R_{CPO}$ (Mehrabadi & Cowin, 1990):

$$R_{CPO\_K} = \begin{bmatrix} R_{11}^2 & R_{12}^2 & R_{12}^2 & \sqrt{2}R_{12}R_{13} & \sqrt{2}R_{11}R_{13} & \sqrt{2}R_{11}R_{12} \\ R_{21}^2 & R_{22}^2 & R_{23}^2 & \sqrt{2}R_{22}R_{23} & \sqrt{2}R_{21}R_{23} & \sqrt{2}R_{21}R_{22} \\ R_{31}^2 & R_{32}^2 & R_{33}^2 & \sqrt{2}R_{32}R_{33} & \sqrt{2}R_{31}R_{33} & \sqrt{2}R_{31}R_{32} \\ \sqrt{2}R_{21}R_{31} & \sqrt{2}R_{22}R_{32} & \sqrt{2}R_{23}R_{33} & R_{22}R_{33} + R_{23}R_{32} & R_{21}R_{33} + R_{23}R_{31} & R_{21}R_{32} + R_{22}R_{31} \\ \sqrt{2}R_{11}R_{31} & \sqrt{2}R_{12}R_{32} & \sqrt{2}R_{13}R_{33} & R_{12}R_{33} + R_{13}R_{32} & R_{11}R_{33} + R_{13}R_{31} & R_{11}R_{32} + R_{12}R_{31} \\ \sqrt{2}R_{11}R_{21} & \sqrt{2}R_{12}R_{22} & \sqrt{2}R_{13}R_{23} & R_{12}R_{23} + R_{13}R_{22} & R_{11}R_{23} + R_{13}R_{21} & R_{11}R_{22} + R_{12}R_{21} \end{bmatrix}$$

## 3. Movement towards y-direction for the mantle wedge particle

In Figure 7a, from time step 13 to 20, we see transition from a girdle-like texture to a point-like texture where the maximum is moving towards the y-direction (Figure 1). From the velocity gradient tensors in Table 2 from time step 13 to 20, we can see that this movement can be explained by the $D_{23}$ component, where $D_{23}$ for MDM+AV (normalized by $D_{11}$) is more than ten times larger than $D_{23}$ for ASPECT (D-Rex). $D_{23}$ for MDM+AV also follows a increasing trend during these time steps, showing that the y-direction movement is increasing. Since the velocity gradient of MDM+AV is scaled from the velocity gradient of ASPECT using the ratio between ASPECT strain rate and MDM+AV strain rate which is predicted using the fluidity tensor, we think the y-direction movement reflects the effect of AV.

Figure 1. Principal stresses from deviatoric stress tensors and pole figures of olivine a-axis from time step 13 to 20.

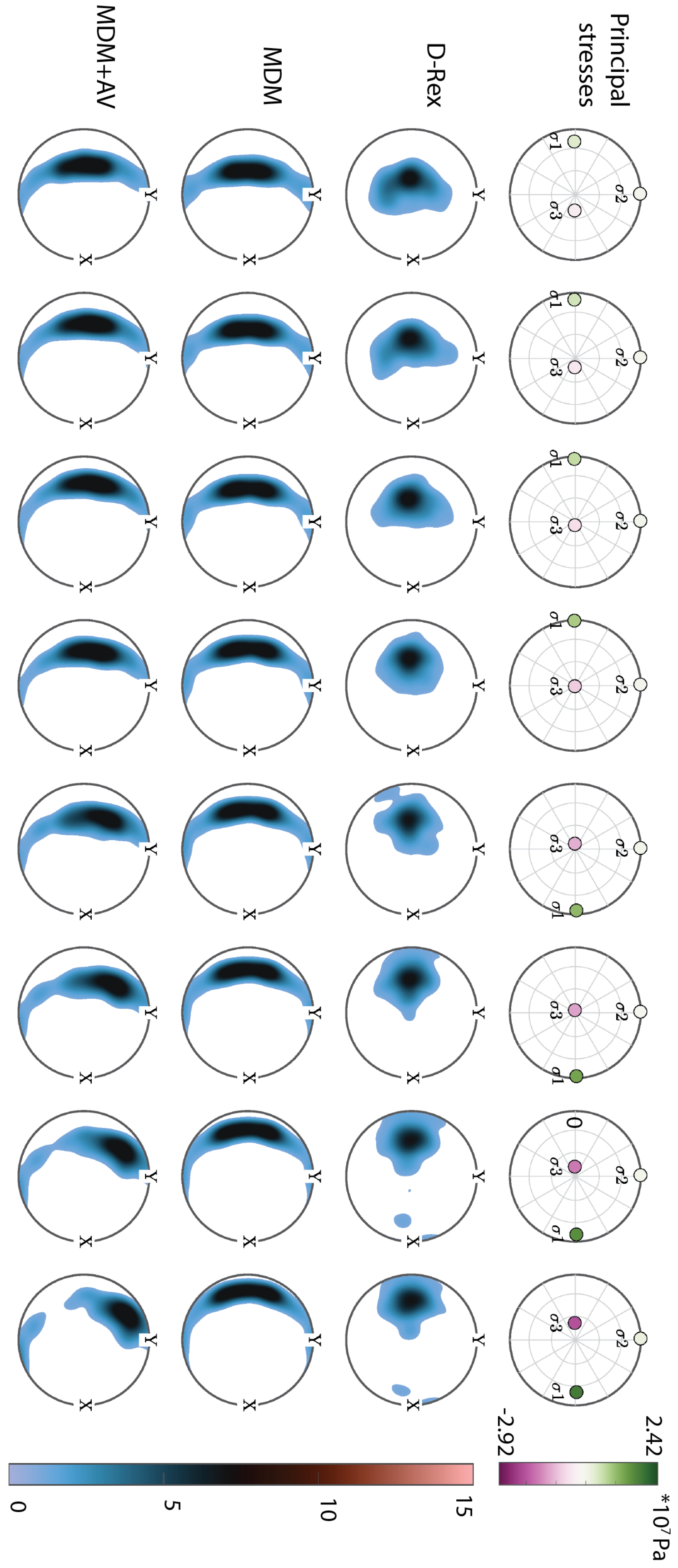

Table 2. Velocity gradient tensors from ASPECT (D-Rex) and MDM+AV that are normalized by the $D_{11}$ component.

| velocity gradient (ASPECT) | | | velocity gradient (MDM+AV) | | |
|---|---|---|---|---|---|
| Time step 13 | | | | | |
| 1 | 0.002422 | 0.23984 | 1 | 0.000445 | 0.238886 |
| 0.037869 | 0.005931 | 0.026333 | 0.006959 | 0.024527 | 0.461423 |
| -1.04064 | -0.00677 | -0.92524 | -1.0365 | -0.1187 | -1.02453 |
| Time step 14 | | | | | |
| 1 | 0.003443 | 0.5303 | 1 | 0.012006 | 0.454329 |
| 0.030515 | 0.005931 | 0.028704 | 0.106414 | 0.037844 | 0.33671 |
| -0.82578 | -0.00676 | -1.03117 | -0.70748 | -0.07932 | -1.03784 |
| Time step 15 | | | | | |
| 1 | 0.003213 | 0.645622 | 1 | 0.022698 | 1.886914 |
| 0.027471 | 0.005215 | 0.026579 | 0.194041 | -0.18287 | 0.173842 |
| -0.70757 | -0.00501 | -0.93244 | -2.06796 | -0.03275 | -0.81713 |
| Time step 16 | | | | | |
| 1 | 0.004321 | 1.073065 | 1 | -0.01835 | 1.764435 |
| 0.025302 | 0.005636 | 0.034418 | -0.10747 | 0.446245 | 0.737777 |
| -0.57036 | -0.00474 | -1.08099 | -0.93784 | -0.1015 | -1.44625 |
| Time step 17 | | | | | |
| 1 | 0.005223 | 0.605768 | 1 | 0.033665 | 0.523586 |
| 0.024695 | 0.006895 | 0.024501 | 0.159165 | -0.05582 | 0.706111 |
| -0.40411 | -0.005 | -0.74474 | -0.34928 | -0.14409 | -0.94418 |
| Time step 18 | | | | | |
| 1 | 0.005523 | 1.114716 | 1 | 0.041765 | 1.236822 |
| 0.023648 | 0.008606 | 0.039695 | 0.17884 | 0.13594 | 0.959895 |
| -0.19413 | -0.00445 | -1.0466 | -0.21539 | -0.10772 | -1.13594 |
| Time step 19 | | | | | |
| 1 | 0.007114 | 2.186298 | 1 | 0.023572 | 2.766975 |
| 0.026023 | 0.011838 | 0.071271 | 0.086232 | 0.55458 | 1.500466 |
| 0.034801 | -0.00468 | -1.42407 | 0.044044 | -0.09851 | -1.55458 |
| Time step 20 | | | | | |
| 1 | 0.009567 | 1.48098 | 1 | 0.066254 | 1.812826 |
| 0.025284 | 0.017826 | 0.064265 | 0.175092 | 0.351911 | 1.509836 |
| 0.429204 | -0.00531 | -1.24557 | 0.525376 | -0.1247 | -1.35191 |

Table 3. Strain rate tensors from ASPECT (D-Rex) and MDM+AV.

| Strain rate (ASPECT) | | | Strain rate (MDM+AV) | | |
|---|---|---|---|---|---|
| Time step 13 | | | | | |
| 1 | 0.020145 | -0.40039 | 1 | 0.003702 | -0.3988 |
| 0.020145 | 0.005931 | 0.009779 | 0.003702 | 0.024527 | 0.171362 |
| -0.40039 | 0.009779 | -0.92524 | -0.3988 | 0.171362 | -1.02453 |
| Time step 14 | | | | | |
| 1 | 0.016978 | -0.14775 | 1 | 0.059207 | -0.12658 |
| 0.016978 | 0.005931 | 0.010971 | 0.059207 | 0.037844 | 0.128696 |
| -0.14775 | 0.010971 | -1.03117 | -0.12658 | 0.128696 | -1.03784 |
| Time step 15 | | | | | |
| 1 | 0.015342 | -0.03098 | 1 | 0.108369 | -0.09053 |
| 0.015342 | 0.005215 | 0.010786 | 0.108369 | -0.18287 | 0.070545 |
| -0.03098 | 0.010786 | -0.93244 | -0.09053 | 0.070545 | -0.81713 |
| Time step 16 | | | | | |
| 1 | 0.014812 | 0.251351 | 1 | -0.06291 | 0.413295 |
| 0.014812 | 0.005636 | 0.014841 | -0.06291 | 0.446245 | 0.318125 |
| 0.251351 | 0.014841 | -1.08099 | 0.413295 | 0.318125 | -1.44625 |
| Time step 17 | | | | | |
| 1 | 0.014959 | 0.100824 | 1 | 0.096416 | 0.087146 |
| 0.014959 | 0.006895 | 0.00975 | 0.096416 | -0.05582 | 0.281009 |
| 0.100824 | 0.00975 | -0.74474 | 0.087146 | 0.281009 | -0.94418 |
| Time step 18 | | | | | |
| 1 | 0.014585 | 0.460284 | 1 | 0.110301 | 0.510704 |
| 0.014585 | 0.008606 | 0.017621 | 0.110301 | 0.13594 | 0.426097 |
| 0.460284 | 0.017621 | -1.0466 | 0.510704 | 0.426097 | -1.13594 |
| Time step 19 | | | | | |
| 1 | 0.016568 | 1.11054 | 1 | 0.054902 | 1.405498 |
| 0.016568 | 0.011838 | 0.033297 | 0.054902 | 0.55458 | 0.701007 |
| 1.11054 | 0.033297 | -1.42407 | 1.405498 | 0.701007 | -1.55458 |
| Time step 20 | | | | | |
| 1 | 0.017426 | 0.955088 | 1 | 0.120674 | 1.169096 |
| 0.017426 | 0.017826 | 0.029478 | 0.120674 | 0.351911 | 0.692562 |
| 0.955088 | 0.029478 | -1.24557 | 1.169096 | 0.692562 | -1.35191 |

References

Fraters, M. R. T., & Billen, M. I. (2021). On the Implementation and Usability of Crystal Preferred Orientation Evolution in Geodynamic Modeling. *Geochemistry, Geophysics, Geosystems*, *22*(10). https://doi.org/10.1029/2021GC009846

Mehrabadi, M. M., & Cowin, S. C. (1990). Eigentensors of linear anisotropic elastic materials. *The Quarterly Journal of Mechanics and Applied Mathematics*, *43*(1), 15–41. https://doi.org/10.1093/qjmam/43.1.15

Signorelli, J., Hassani, R., Tommasi, A., & Mameri, L. (2021). An effective parameterization of texture-induced viscous anisotropy in orthotropic materials with application for modeling geodynamical flows. *Journal of Theoretical, Computational and Applied Mechanics*, 6737. https://doi.org/10.46298/jtcam.6737